

Analog of Foucault precession in two-dimensional quantum harmonic oscillators with Berry curvature

D. D. Solnyshkov^{1,2}, I. Septembre,¹ K. Ndiaye,¹ and G. Malpuech¹

¹*Institut Pascal, PHOTON-N2, Université Clermont Auvergne, CNRS, Clermont INP, F-63000 Clermont-Ferrand, France*

²*Institut Universitaire de France (IUF), F-75231 Paris, France*



(Received 21 December 2022; revised 13 June 2023; accepted 16 October 2023; published 27 October 2023)

The geometric phase plays a key role both in the rotation of the Foucault pendulum and in the anomalous Hall effect (AHE), where an accelerated wave packet shows a transverse motion induced by the Berry curvature. Here, we show that the motion of quantum particles described by a spin-orbit-coupling Hamiltonian showing nonzero Berry curvature and placed in a two-dimensional harmonic-oscillator potential in real space exhibits Foucault precession. The plane of the oscillations rotates with time. The rotating pendulum configuration enhances the spatial deviation with respect to the AHE case, simplifying its observation and allowing high-precision measurements of the Berry curvature. We show how the nonadiabaticity and anharmonicity determine the maximal rotation angle and find the optimal conditions for the observations.

DOI: [10.1103/PhysRevB.108.144306](https://doi.org/10.1103/PhysRevB.108.144306)

I. INTRODUCTION

The Foucault pendulum was suggested and implemented by Léon Foucault in 1851 to demonstrate Earth's rotation [1]. It is one of the most widely known experiments [2], demonstrated in many science museums around the world [3]. However, it is much less known that it was also Léon Foucault who, inspired by his pendulum's working principle, created the first gyroscope [4,5]. Contrary to the Foucault pendulum, which mostly remains a brilliant demonstration, the gyroscopes, based on the same basic property, have become extremely widespread. Now they are used for the orientation at all scales, from smartphones [6] to the International Space Station [7]. Moreover, some of the most efficient microscopic implementations of the gyroscopes [8] use oscillations instead of rotation [9], thus coming back to the Foucault pendulum (on a chip) [10]. Recently, an implementation of the Foucault pendulum based on a Bose-Einstein condensate in a synthetic rotational field has been suggested [11].

Geometric phases are quite widespread in physics [12]. Such phase plays a key role in the Foucault pendulum by determining its rotation versus latitude [3,13–17]. The geometric phase is accumulated during the transport around Earth at a given latitude. The associated rotation angle can be linked with an integral of Earth's curvature. The Foucault pendulum can also be used to measure Earth's gravitomagnetic field [18] or the Lense-Thirring effect [19]. From an even broader perspective, since any motion due to noninertial pseudoforces can be viewed as a space-time curvature in general relativity according to the Einstein's equivalence principle [20], any rotation of the Foucault pendulum is always due to a certain curvature (Earth's curvature, space-time curvature, or some other), and thus the Foucault pendulum can be seen as a device for the measurement of curvatures and of the associated geometric phases.

The Berry (Pancharatnam) phase is another well-known example of a geometric phase, studied in quantum [21–23]

and classical systems [14]: it stems from the curvature of the eigenstates over the parameter space of the Hamiltonian (e.g., reciprocal space). This phase and the associated Berry curvature are key concepts in modern topological physics, being involved in the optical spin Hall effect [24–27], topological insulators [28–30], lasers [31], and optical isolators [32,33]. The Berry curvature can be seen as a gauge field [22,34], an equivalent of a magnetic field in the reciprocal space. As such, it affects the spatial trajectories of accelerated particles via the anomalous Hall Effect (AHE) [35], recently directly measured in a photonic system [36]. Two general two-dimensional (2D) Hamiltonians characterized by a nonzero Berry curvature for the eigenstates of their bands are the Dirac Hamiltonian (winding 1) and the TE-TM Hamiltonian (winding 2). The former is the most well-known Hamiltonian exhibiting Berry curvature and representing a reference case. Its implementations include 2D electron gas with Rashba spin-orbit coupling (SOC) [37] and Zeeman splitting [38,39], 2D transition-metal dichalcogenides (TMDs) [40,41], biased bilayer graphene [42], and photonic quantum valley Hall effect [43]. The TE-TM Hamiltonian describes the inherent topology of the photonic modes associated with their vectorial nature [44]. It describes the propagation of light beams in any inhomogeneous system, for example, for paraxial beams of light [44–46] and in microcavities [26,47]. In recent studies it appears combined with non-Hermiticity [48–50]. Photonic systems allow direct access to the dispersion of modes, their Berry curvature distribution, and real-space dynamics of wave packets in various potentials, such as 2D harmonic traps [51,52]. With linear birefringence, they also allow implementing the 2D massive Dirac Hamiltonian [36,53,54].

In this work, we study 2D particles described by a SOC Hamiltonian with nonzero Berry curvature and placed in a 2D parabolic potential, where they oscillate. The accumulation of the associated geometric (Berry) phase during the particle acceleration by the potential leads to the rotation of the

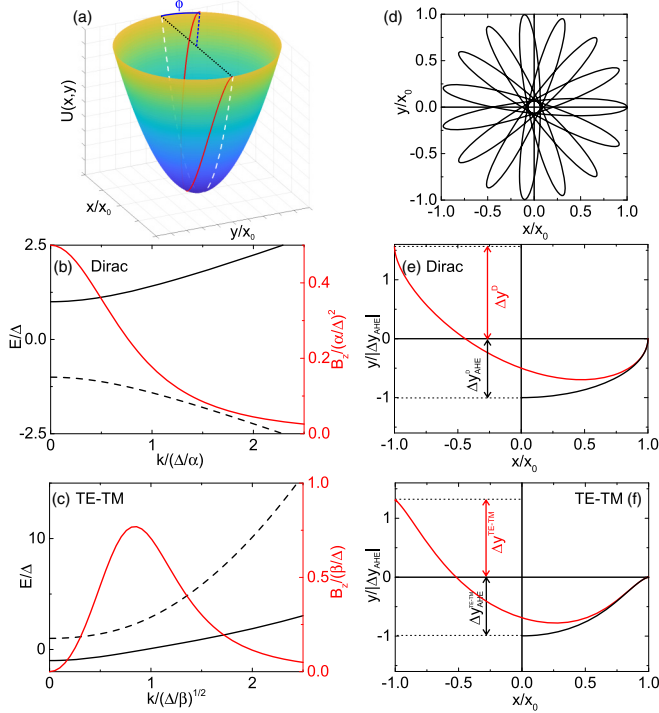


FIG. 1. (a) Three-dimensional sketch of a parabolic potential and the wave packet trajectory (red curve) over half oscillation period with a deviation Δy corresponding to an angular shift of ϕ (blue line). (d) Trajectory of a Berry-Foucault pendulum in the case of a Dirac Hamiltonian (1), completely equivalent to a Foucault pendulum (reduced units). Energy spectrum (black) and Berry curvature (red) profile for the (b) Dirac Hamiltonian (1) and the (c) TE-TM (2) Hamiltonian. Black solid lines are the branches of interest. Comparison between the AHE Δy_{AHE} (black) and the Berry-Foucault deviation Δy (red) for (e) Dirac and (f) TE-TM.

plane of the oscillations, as in the Foucault pendulum, but without any noninertiality. We call this system the Berry-Foucault pendulum. We consider two above-mentioned SOC Hamiltonians (Dirac and TE-TM) in two dimensions, showing how the AHE can be amplified in the Foucault pendulum configuration, allowing to measure the Berry curvature with a high precision and even in systems, where the eigenstates are not directly accessible. We also study the limits of the Berry-Foucault pendulum operation set by the nonadiabaticity and the anharmonicity, determining the optimal configuration for measurements.

II. THE MODEL

We consider a spinor particle described by a Hamiltonian H_{SOC} including a SOC term inducing a nonzero Berry curvature. We study the oscillations of a wave packet launched at $x = x_0$ in a 2D parabolic potential $U_{ho}(x, y) = \xi(x^2 + y^2)I_2/2$ [Fig. 1(a)], where I_2 is the identity matrix. The full Hamiltonian reads $H = H_{\text{SOC}} + U$. The usual AHE configuration corresponds to U being a one-dimensional (1D) potential with a constant gradient, with the Berry curvature leading to lateral deviation [35]. In our case, the interplay between the deviation induced by the Berry curvature and the effect of the 2D

potential leads to a complex trajectory [see Fig. 1(a), red line], characterized by the rotation angle ϕ of the oscillation plane (blue line).

We consider two different cases for H_{SOC} . The first one is the massive Dirac Hamiltonian (with its two bands originally introduced for particles and antiparticles, which implies a nonzero Berry curvature for an ordinary electron [55] and the corresponding anomalous Hall effect [56], but also describing the electron spin in spintronics [38,39] or the sublattice pseudospin in topological valleys [40–43]).

The Dirac Hamiltonian written in reciprocal space reads

$$\hat{H}_{\text{Dirac}} = \begin{pmatrix} +\Delta_D & \alpha k e^{-i\varphi} \\ \alpha k e^{i\varphi} & -\Delta_D \end{pmatrix}, \quad (1)$$

where k is the 2D wave vector modulus, φ its polar angle, α is related to Rashba SOC [38] or the Fermi velocity [40,42], and Δ_D is the time-reversal symmetry-breaking term (Zeeman splitting) or “staggering” term in 2D materials. In the original Dirac equation, $\Delta_D = m_e c^2$, $\alpha = \hbar c$, where m_e is the electron mass and c is the speed of light, which is why the anomalous Hall effect of a free electron is so small (of the order of the Compton wavelength, $\approx 2.4 \times 10^{-12}$ m). The Berry curvature of the lower band of the Dirac Hamiltonian reads [57]: $B_z^D(k) = \alpha^2 \Delta_D / 2(\alpha^2 k^2 + \Delta_D^2)^{3/2}$.

The second case we take for H_{SOC} is the TE-TM Hamiltonian with a Faraday (Zeeman) term describing the transverse dynamics of massive photons (mass m). Here the two bands describe the photon polarization either in the paraxial configuration [44–46] or in microcavities [26,47,48]. It reads

$$\hat{H}_{\text{TE-TM}} = \begin{pmatrix} \frac{\hbar^2 k^2}{2m} + \Delta & \beta k^2 e^{-2i\varphi} \\ \beta k^2 e^{2i\varphi} & \frac{\hbar^2 k^2}{2m} - \Delta \end{pmatrix}, \quad (2)$$

with TE-TM splitting magnitude β and a time-reversal symmetry-breaking term Δ (Faraday effect). The Berry curvature of the lower band reads [58]: $B_z^{\text{TE-TM}}(k) = 2\Delta\beta^2 k^2 / (\Delta^2 + \beta^2 k^4)^{3/2}$.

Figures 1(b) and 1(c) show the two band dispersions and the lower band Berry curvature for the two Hamiltonians. The Dirac Hamiltonian is well described by a parabolic dispersion at $k \approx 0$ and exhibits the maximum of the Berry curvature at the same point, while the TE-TM Hamiltonian has the maximum of the Berry curvature at $k = (\Delta/\sqrt{2}\beta)^{1/2} \neq 0$, where the dispersion is nonparabolic.

The full problem contains H_{SOC} and a spatially varying potential. The Hamiltonians (1) and (2) are converted to real space using $\mathbf{k} = -i\nabla$. Combined with the harmonic potential $U_{ho}(x, y)$, they give the complete Hamiltonians $H_{D,HO}$ and $H_{\text{TE-TM},HO}$. We also use a 1D potential $U_1 = \zeta x$ with a constant gradient ζ as a reference for usual AHE configuration, giving complete Hamiltonians $H_{D,1}$ and $H_{\text{TE-TM},1}$. We start by using a semiclassical description of the wave packet motion, which allows us to treat the problem analytically.

III. SEMICLASSICAL DESCRIPTION

In the adiabatic limit, the semiclassical motion of a wave packet in presence of potential $U(\mathbf{r})$ and of Berry curvature

$B(\mathbf{p})$ was derived by Sundaram and Niu [35]:

$$\dot{\mathbf{p}} = -\nabla U, \quad (3)$$

$$\dot{\mathbf{r}} = \nabla_p E + \hbar^{-1} \dot{\mathbf{p}} \times \mathbf{B}(\mathbf{p}), \quad (4)$$

where \mathbf{r} is the coordinate of the wave packet center of mass, \mathbf{p} is the momentum of the wave packet center of mass ($\mathbf{p} = \hbar\mathbf{k}$), and the Berry curvature $\mathbf{B}(\mathbf{p})$ appears as a ‘‘reciprocal-space magnetic field.’’ These equations assume the wave packet to be in a single band [solid line in Figs. 1(b) and 1(c)]. The analogy between the Berry magnetic force and the magnetic Lorentz force is not full in the general case. However, for a 2D harmonic oscillator and a constant Berry curvature (Dirac Hamiltonian, $k \approx 0$), it is possible to obtain a complete reciprocity between the two effects described by terms proportional to $\mathbf{p} \times \mathbf{B}_{\text{magn}}$ and $\mathbf{r} \times \mathbf{B}$ in the equations for $\dot{\mathbf{p}}$ and $\dot{\mathbf{r}}$, respectively (see Appendix A for details). There is also a complete analogy between the magnetic Lorentz force $\approx \mathbf{v} \times \mathbf{B}_{\text{magn}}$ and the Coriolis force $\approx \mathbf{v} \times \boldsymbol{\Omega}_{\text{rot}}$ acting on the Foucault pendulum. From this analysis, we can already conclude that, with the Dirac Hamiltonian, the trajectory of a wave packet in the 2D parabolic potential is equivalent to the one of a Foucault pendulum (Appendix A). The corresponding trajectories, identical in both cases (Foucault and Berry-Foucault), are shown in Fig. 1(d). The TE-TM case with a variable Berry curvature shows, of course, a different behavior.

The next step is to quantitatively compare the wave packet deviation in the usual AHE, where $U = \zeta x$, with the one occurring during one period in the 2D harmonic-oscillator case. We take the initial condition $x_0 > 0$, $y_0 = 0$, $\mathbf{p}_0 = 0$. In the AHE case with acceleration along x , the deviation along y reads:

$$\Delta y_{\text{AHE}} = \int_0^{k_{\text{max}}} B(k_x) dk_x, \quad (5)$$

where k_{max} is the maximal wave vector achieved during the acceleration. In the Dirac case with $H_{D,1}$ it reads $\Delta y_{\text{AHE}}^D = \alpha^2 k_{\text{max}} / 2\Delta_D (\alpha^2 k_{\text{max}}^2 + \Delta_D^2)^{1/2}$. The deviation grows with k_{max} up to the maximal deviation $\alpha / 2\Delta_D$. For small k_{max} it can be rewritten as $\Delta y_{\text{AHE}}^D = B(0)k_{\text{max}}$, where $B(0) = \alpha^2 / 2\Delta_D^2$ is the Berry curvature at $k = 0$. For the TE-TM case with $H_{\text{TETM},1}$, the AHE drift is expressed via the hypergeometric function. For small k_{max} it reads $\Delta y_{\text{AHE}}^{\text{TE-TM}} \approx 2\beta^2 k_{\text{max}}^3 / 3\Delta^2$.

We then consider the 2D harmonic-oscillator case with $H_{D,\text{HO}}$ and $H_{\text{TETM},\text{HO}}$ for one half-oscillation along x assuming $\Delta y \ll x_0$, which allows us to decouple x and y . In that case, Eqs. (4) for $y(t)$ and $p_y(t)$ become equivalent to a driven harmonic oscillator with an external force defined by $\dot{p}_x B_z(p_x)$. Using the Green’s function approach (Appendix A), we find the ratios of the deviations $\Delta y^D / \Delta y_{\text{AHE}}^D = -\pi/2$ and $\Delta y^{\text{TE-TM}} / \Delta y_{\text{AHE}}^{\text{TE-TM}} = -3\pi/8$. In both cases, the deviation for a half-period is comparable in magnitude to the AHE deviation, but has an *opposite* direction. The AHE and a half-period Berry-Foucault pendulum trajectories are shown in Figs. 1(e) and 1(f). At early time both coincide, but then the 2D parabolic potential provides its own lateral acceleration, bringing a lateral deviation opposite to the initial one of the AHE, as in the original Foucault pendulum [59] (accounting for the real-reciprocal space mapping, see Appendix A).

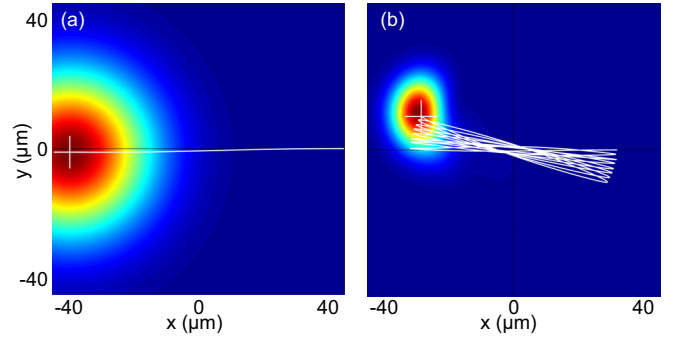


FIG. 2. Amplification of the Berry curvature effect. (a) Reference: AHE ($H_{\text{TETM},1}$); (b) Amplification: Berry-Foucault pendulum ($H_{\text{TETM},\text{HO}}$). False color—particle density $n = |\psi|^2$, white line—center-of-mass trajectory.

For small wave vectors, k_{max} in the harmonic-oscillator case can be obtained from x_0 (the oscillation amplitude) as $k_{\text{max}}^D \approx x_0 \sqrt{\Delta_D \xi} / \alpha$ and $k_{\text{max}}^{\text{TE-TM}} \approx x_0 \sqrt{\xi m} / \hbar$. Thus, the angles of rotation of the oscillation plane for $H_{D,\text{HO}}$ and $H_{\text{TETM},\text{HO}}$ for a half-period are

$$\phi^D = \arctan \frac{\Delta_y^D}{x_0} \approx \frac{\pi \alpha \sqrt{\xi}}{4\Delta_D^{3/2}}, \quad (6)$$

which in this limit does not depend on x_0 , and

$$\phi^{\text{TE-TM}} \approx \frac{\pi \beta^2 \xi^{3/2} m^{3/2} x_0^2}{4\hbar^3 \Delta^2}, \quad (7)$$

which grows quadratically with x_0 . The comparison of the Dirac case with the Foucault phase due to Earth’s curvature is provided in Appendix B. The similarity of the two expressions is due to the geometric origin of the effect (anholonomy).

IV. NUMERICAL SIMULATIONS

The next step is to go beyond the semiclassical picture considering that we are dealing with spatially extended wave packets and not classical particles. For this, we perform numerical simulations with a time-dependent Schrödinger equation $i\hbar \partial \psi / \partial t = \hat{H} \psi$ for different full Hamiltonians \hat{H} , starting with an initial Gaussian wave packet characterized by a root-mean-square width σ . Figure 2 shows these simulations for the TE-TM Hamiltonian for the usual AHE [$H_{\text{TETM},1}$, Fig. 2(a)] and the Berry-Foucault pendulum [$H_{\text{TETM},\text{HO}}$, Fig. 2(b)]. The parameters used [60] are typical for GaAs-based microcavities [61]. The AHE, resulting from a constant potential gradient ζ , requires working with a large wave packet: the scale of the effect is much smaller than the wave packet size:

$$\Delta y \ll \sigma. \quad (8)$$

Even if a smaller wave packet is taken initially, it necessarily expands over time, linearly for large t [62]. For realistic parameters the AHE appears as a slight drift with respect to the straight trajectory (white line).

In the Berry-Foucault pendulum defined by $H_{\text{TETM},\text{HO}}$ [Fig. 2(b)], the parameter of the harmonic potential ξ

determines the size of the Gaussian wave packet:

$$\sigma = \sqrt{\hbar/m\omega} = \sqrt{\hbar/\sqrt{\xi}m}. \quad (9)$$

The wave packet does not expand or shrink over time [63]. This allows us to operate with wave packets much smaller than for the AHE, as immediately visible in Fig. 2(b). Moreover, if the Berry-Foucault pendulum carries out Q oscillations, the anomalous Hall deviation is amplified accordingly, allowing the final deviation to exceed the wave packet size:

$$Q\Delta y > \sigma. \quad (10)$$

It is possible to have an accumulation of the AHE deviation in the constant potential gradient case, if the wave packet crosses the edges of the Brillouin zone in a periodic lattice. This corresponds to the well-known phenomenon of Bloch oscillations [64]. However, in this case both the AHE deviation and the wave packet size increase linearly with time, so that the AHE drift remains smaller than the wave packet size (see Appendix C for details). Moreover, Bloch oscillations are impossible in natural electronic bands (due to their large energy size) and limited by approximately 10 oscillations in artificial electronic [64], atomic [65,66], and photonic [67] systems, due to disorder and Landau-Zener tunneling to upper bands. This limits the possibilities of the AHE amplification due to the Bloch oscillations. The Bloch oscillation approach cannot be used at all for the studies of the Berry curvature via AHE in continuous systems [36] (without Brillouin zones), or for systems with opposite Berry curvature in two valleys; that is, trivial band topology (e.g., TMDs).

We then compare the analytical results for the half-period rotation angle (6) and (7) with those of Schrödinger equation with $H_{D,HO}$ and $H_{TE-TM,HO}$ (see Ref. [68] for parameters). Figures 3(a) and 3(b) shows the x_0 dependence. The Schrödinger equation reproduces the limit of ϕ^D for $x_0 \rightarrow 0$. The quadratic dependence of ϕ^{TE-TM} is well reproduced at low x_0 as well.

V. LIMITATIONS

The maximal number of oscillations Q is determined by the Q factor of the oscillator. This limitation is determined by the nonadiabaticity and by the anharmonicity. Nonadiabaticity is represented by the transfer of the wave packet from the initial band to the other band because of the finite acceleration. Anharmonicity is induced by the nonparabolic character of the dispersion. Similar limitations exist also for the classical Foucault pendulum, which deviates from perfectly planar oscillations [69], unless suppression devices are used [5]. Experimentally, the simplest tunable variable is x_0 .

A convenient tool [70] to estimate the nonadiabaticity is the quantum metric [71] g_{ij} , determining the overlaps between the eigenstates $|\langle\psi(\mathbf{k})|\psi(\mathbf{k}+\mathbf{d}\mathbf{k})\rangle|^2 = 1 - \sum_{i,j} g_{ij}d\mathbf{k}_i d\mathbf{k}_j$. For the Dirac Hamiltonian at $k \approx 0$, $g_{kk} = \alpha^2/4\Delta_D^2$ (radial component) and the nonadiabatic fraction [70] can be estimated as $\sqrt{f_{NA}} \approx \sqrt{g_{kk}k_{\max}}$ (see Appendix D). Using the expression for k_{\max} , we obtain $f_{NA}^D \approx \xi x_0^2/4\Delta_D$. At each half period, the nonadiabatic fraction escapes the confinement due to the opposite sign of

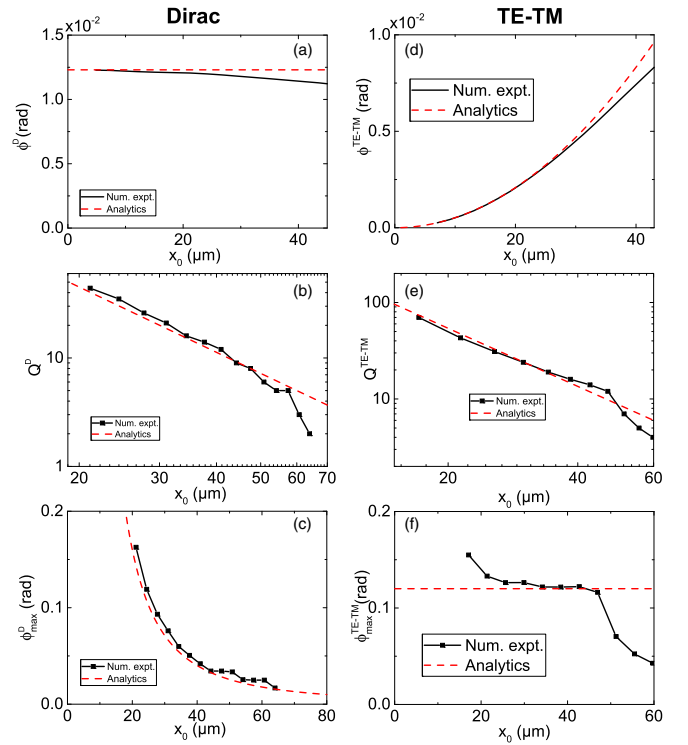


FIG. 3. Berry-Foucault pendulum for the Dirac $H_{D,HO}$ and TE-TM $H_{TE-TM,HO}$ Hamiltonians respectively: (a), (d) half-period rotation angle ϕ ; (b), (e) Q factor; (c), (f) maximal rotation angle ϕ_{\max} , all as a function of initial position x_0 . Black lines and points—numerical experiment, red dashed lines—analytics.

the mass of the second band. The nonadiabaticity thus directly determines the losses of the wave packet (see Appendix D for anharmonicity). This allows us to determine the Q factor of the oscillator and the maximal rotation angle ϕ_{\max} as

$$Q^D = \frac{4\Delta_D}{\xi x_0^2}, \quad \phi_{\max}^D = \frac{\pi\alpha}{\sqrt{\xi}\Delta_D x_0}. \quad (11)$$

For the TE-TM Hamiltonian, $g_{kk} = \beta^2 k^2/\Delta^2$. The nonadiabatic fraction turns out to be negligible with respect to the anharmonicity (Appendix D). The nonparabolicity of dispersions makes the states of the harmonic potential unequally spaced in frequency. The oscillating wave packet is a linear superposition of these eigenstates. For small x_0 , anharmonicity simply provokes a decay of the wave packet, allowing to write perturbatively: $Q = \omega/\Delta\omega$, where $\omega = \sqrt{\xi/m}$ is the mean frequency of the harmonic oscillator and $\Delta\omega$ is due to the mass difference between $k=0$ and $k=k_{\max}$. Beyond a critical x_0 , the deviation from the ideal harmonic oscillator quickly destroys the wave packet (Appendix E).

These analytical results are compared with the results of numerical experiments in Figs. 3(b) and 3(c), with all panels demonstrating a good agreement. The Q factor $Q(x_0)$ is plotted in Fig. 3(b) on a double log scale, demonstrating the power-law decay up to critical x_0 , as predicted by (11). Accordingly, the maximal rotation angle also decays with x_0 [Fig. 3(c)].

For the TE-TM Hamiltonian, $m(k) \approx m(1 + 6\beta^2 k^2 m / \hbar^2 \Delta)$, which gives

$$Q^{\text{TE-TM}} \approx \frac{\hbar^4 \Delta}{6\beta^2 m^2 \xi x_0^2}, \quad \phi_{\text{max}}^{\text{TE-TM}} \approx \frac{\pi \hbar \omega}{12 \Delta}. \quad (12)$$

The maximal rotation angle therefore does not depend on the initial position x_0 , contrary to the Dirac case, where it was decaying with x_0 . Moreover, it does not depend on the TE-TM splitting value β .

The Q factor $Q^{\text{TE-TM}}$ versus x_0 is plotted in Fig. 3(e) and compared with Schrödinger simulations. It shows an excellent agreement up to a critical x_0 value. With realistic parameters [60], Q can reach values as high as 10^2 . The total rotation angle $\phi_{\text{max}}^{\text{TE-TM}}$ is plotted in Fig. 3(f) versus x_0 , showing a good agreement with the analytical estimate for small x_0 up to the same critical cutoff x_0 value (see Appendix E).

Another important parameter for experiments in systems with finite lifetime τ is the frequency of the Berry-Foucault precession, which can be found as $\Omega = 2\phi\omega$. Within the same limit as before, it gives $\Omega \sim \pi \beta^2 \xi^2 m x_0^2 / 2\hbar^3 \Delta^2$. One could expect $\tau \gg \Omega^{-1}$ for the experiment to be carried out. However, the polaritonic wave packets can be re-amplified from excitonic reservoir [72], similar to the classical Foucault pendulums accelerated electromagnetically in museums [5]. We therefore consider the condition $\tau \gg \Omega^{-1}$ to be less stringent than the other limitations discussed above.

VI. DISCUSSION AND CONCLUSIONS

Parabolic potential traps are available in many systems, where the Berry curvature and topological effects are studied: in electronics (2D quantum dots [73]), cold atoms [74], and photonics [51,52]. Moreover, the center-of-mass oscillations in harmonic traps (dipole mode) were experimentally shown to be very robust, showing no signs of decay after more than ≈ 250 oscillations [75] (without spin-orbit coupling). This makes the Berry-Foucault configuration favorable for Berry curvature measurements in many systems.

The Berry-Foucault pendulum allows us to improve the precision of the transport measurements [76–78] of the Berry curvature by the factor Q (see Appendix G). This would mean reducing the 10% uncertainty on the Berry curvature in Ref. [36] down to 0.1% with $Q = 100$ from Fig. 3, a significant improvement. Its limit is set by $\Delta > \beta/\sigma^2 = 4\pi^2 \beta \sqrt{\xi m} / \hbar$ (wave packet size should be smaller than the Berry curvature variation scale).

To conclude, we have demonstrated that the Berry curvature leads to Foucault precession for a harmonic oscillator with spin-orbit coupling. We have studied two most well-known Hamiltonians with SOC and determined the Q factor and the maximal rotation angle. The Berry-Foucault pendulum can be used for high-precision curvature measurements close to the band extrema.

ACKNOWLEDGMENTS

We acknowledge the support of the European Union's Horizon 2020 program, through a FET Open research

and innovation action under Grant Agreement No. 964770 (TopoLight), project ANR Labex GaNEXT (ANR-11-LABX-0014), and of the ANR program “Investissements d’Avenir” through the IDEX-ISITE initiative 16-IDEX-0001 (CAP 20-25).

APPENDIX A: THE ANOMALOUS HALL EFFECT IN THE BERRY-FOUCAULT PENDULUM CONFIGURATION

The goal of this section is first to establish the analogy between the motion of quantum particles described by a spin-orbit-coupling Hamiltonian showing nonzero Berry curvature, and placed in a real space 2D harmonic-oscillator potential with the trajectories of the Foucault pendulum.

We then find analytical expressions for the deviations of the center of mass trajectory due to the combined effect of the anomalous velocity induced by the Berry curvature and the acceleration of the 2D potential for one (half period) oscillation.

1. Equivalence

First, we note that there is a complete analogy between the noninertial Coriolis force $\mathbf{F}_{\text{Cor}} = 2m(\mathbf{v} \times \boldsymbol{\Omega})$ and the magnetic part of the Lorentz force $\mathbf{F}_{\text{Lor}} = q(\mathbf{v} \times \mathbf{B})$: both are proportional to a vector product of the velocity \mathbf{v} and a constant pseudovector (rotation angular frequency $\boldsymbol{\Omega}$ or magnetic field \mathbf{B}). This allows us to state that a Foucault pendulum trajectory is similar to the motion of a charged classical particle in a parabolic potential in presence of a constant magnetic field.

In contrast, the analogy between the transverse velocity of the anomalous Hall effect and the Lorentz force is not full in the general case: the two contributions appear differently in the equations of motion. Indeed, a magnetic field can be incorporated into the Hamiltonian as a vector potential \mathbf{A} : $H_{\text{mag}} = (\mathbf{p} - e\mathbf{A})^2 / 2m$ containing the term $\mathbf{p} \cdot \mathbf{A}$, whose reciprocal term should be $\mathbf{r} \cdot \mathbf{A}$, whereas the Berry curvature would correspond to a term $\dot{\mathbf{p}} \cdot \mathbf{A}$ instead. This shows up in the fundamental difference of trajectories between the ordinary Hall effect (circular cyclotron orbits in 2D) and the AHE (finite deviation of the curve).

Nevertheless, if we take a harmonic oscillator with a constant Berry curvature (Dirac Hamiltonian, $k \approx 0$) that can be considered as a correction, it is possible to obtain complete reciprocity between the two effects. The equations of motion for this system write:

$$\dot{\mathbf{p}} = -\xi \mathbf{r}, \quad (A1)$$

$$\dot{\mathbf{r}} = \frac{\mathbf{p}}{m} + \hbar^{-1} \dot{\mathbf{p}} \times \mathbf{B}. \quad (A2)$$

We use the first of the two equations, $\dot{\mathbf{p}} = -\xi \mathbf{r}$, and insert it into the second one:

$$\dot{\mathbf{p}} = -\xi \mathbf{r}, \quad (A3)$$

$$\dot{\mathbf{r}} = \frac{\mathbf{p}}{m} - \hbar^{-1} \xi \mathbf{r} \times \mathbf{B}. \quad (A4)$$

Then the symmetry of Hamilton's equations of motion

$$\dot{p}_i = -\frac{\partial H}{\partial r_i}, \quad (\text{A5})$$

$$\dot{r}_i = \frac{\partial H}{\partial p_i}, \quad (\text{A6})$$

with respect to a substitution $\mathbf{r} \longleftrightarrow -\mathbf{p}$ (in our particular case, $\mathbf{r}' = -\mathbf{p}/m$, $\mathbf{p}' = \xi\mathbf{r}$) allows establishing a full analogy between the ordinary Foucault pendulum and the Berry-Foucault pendulum in the Dirac case. Indeed, with this substitution the equations write:

$$\dot{\mathbf{r}}' = \frac{\mathbf{p}'}{m}, \quad (\text{A7})$$

$$\dot{\mathbf{p}}' = -\xi\mathbf{r}' - \hbar^{-1}\xi\mathbf{p}' \times \mathbf{B}, \quad (\text{A8})$$

which, since the Berry curvature is approximately constant, corresponds to the equations of motion for a charged harmonic oscillator in a constant magnetic field or for a harmonic oscillator in a noninertial system rotating with a frequency $\Omega = -\xi\mathbf{B}/2\hbar$.

We have therefore established a full mathematical equivalence between the semiclassical equations of motion for a wave packet in a quantum harmonic oscillator with a constant Berry curvature and the classical equations of motion of the Foucault pendulum (harmonic oscillator in a noninertial system of coordinates).

2. Analytical solution for a single oscillation

Our goal is to find an analytical expression for the anomalous Hall drift for a single half-period oscillation in a 2D harmonic-oscillator potential. We assume that the first oscillation takes place along the x axis, and the deviation Δy occurs therefore along the y axis. We assume $\Delta y \ll x_0$ (x_0 is the amplitude of the oscillations), which allows us to decouple x and y , considering $x(t) = x_0 \cos \omega t$ and $p_x(t) = -p_{\max} \sin \omega t$ as known. This allows us to write a system of equations for $y(t)$ and $p_y(t)$ from (A2):

$$\dot{p}_y = -\xi y, \quad (\text{A9})$$

$$\dot{y} = p_y/m - \hbar^{-1}\dot{p}_x B_z(p_x). \quad (\text{A10})$$

Again, thanks to the symmetry of the Hamilton's equations of motion with respect to $\mathbf{r}' = -\mathbf{p}/m$, $\mathbf{p}' = \xi\mathbf{r}$, this system of equations is equivalent to a driven harmonic oscillator with an external force defined by $\dot{p}_x B_z(p_x)$. This is what allows to use the Green's function formalism to find the solution of these equations of motion. This solution is given by

$$\Delta y = -p_{\max} \omega^2 \int_0^{T/2} \cos^2 \omega t' B(p_{\max} \sin \omega t') dt', \quad (\text{A11})$$

with $T = 2\pi/\omega$. The integration gives the coefficients $-\pi/2$ and $-3\pi/8$ given in the main text.

APPENDIX B: THE PRECESSION ANGLE AND THE CURVATURE

Our goal here is to compare the expressions for the angles of rotation of the Berry-Foucault pendulum and the classical Foucault pendulum. For the latter, it is well known that Earth's

curvature and the associated geometric phase are important for the calculation of the rotation angle, together with the main contribution coming from the noninertial nature of the reference frame (Earth's rotation). For the Berry-Foucault pendulum, it is the Berry curvature which totally determines the rotation angle. It is therefore instructive to compare both.

In the main text, we have obtained the angle of rotation of the Berry-Foucault pendulum with the Dirac Hamiltonian (for one half period):

$$\phi^D \approx \frac{\pi\alpha\sqrt{\xi}}{4\Delta_D^{3/2}}. \quad (\text{B1})$$

This result can be directly compared with the rotation angle of the classical Foucault pendulum, which reads for 1 day

$$\phi_{\text{day}} = 2\pi - \int \kappa dS = 2\pi \left(1 - R^2 \int_0^\theta \kappa(\theta') \sin \theta' d\theta' \right), \quad (\text{B2})$$

where $\theta = \pi/2 - \varphi$ is the polar angle corresponding to the latitude φ . The first term is due to the noninertial nature of the system (the rotation of Earth), whereas the second one is due to the curvature κ of Earth's surface. The importance of the Foucault pendulum in popular education is therefore doubled: it allows demonstrating Earth's rotation and Earth's curvature, providing two important arguments against the modern "Flat Earth" trend [79].

This last term is also called the phase of the Foucault pendulum (we remind that it is not the total rotation angle, but only a negative contribution to it, due to Earth's curvature):

$$\phi_F = \int \kappa dS. \quad (\text{B3})$$

For a constant curvature of a sphere $\kappa = 1/R^2$, one recovers the famous formula appearing in the total angle of the Foucault's pendulum rotation:

$$\phi_{\text{day}} = 2\pi[1 - (1 - \cos \theta)] = 2\pi \sin \varphi. \quad (\text{B4})$$

However, if we imagine that the curvature is not constant, but only approximately constant around $\theta = 0$ (which is indeed the case for Earth), we can write $\kappa(\theta) \approx \kappa(0)$. Then we obtain an expression similar to the one of the anomalous Hall drift:

$$\phi_{\text{day}} = 2\pi - 2\pi R^2 \kappa(0)(1 - \cos \theta). \quad (\text{B5})$$

Using the series expansion for $\cos(\theta)$ and knowing that the rotation angle for 1 half oscillation is proportional to the rotation angle for 1 day, we obtain the curvature-induced correction (the Foucault phase)

$$\phi_1 \sim \kappa(0)(R\theta)^2. \quad (\text{B6})$$

This compares directly with the rotation angle of the Berry-Foucault pendulum in the Dirac case,

$$\phi^D \sim B(0)k_{\max}^2, \quad (\text{B7})$$

where $B(0)$ is the Berry curvature maximum.

Naturally, the curvature-induced contributions write similarly in both cases: as a product of the curvature and a surface in the parameter space. We note, however, that for the Berry-Foucault pendulum the curvature is the only source of

precession, whereas for the original Foucault pendulum it is a negative correction, reducing the rotation angle with respect to the one expected in a noninertial system, 2π in 24 hours.

APPENDIX C: ANOMALOUS HALL EFFECT IN BLOCH OSCILLATIONS: WAVE-PACKET GROWTH

In this section, we analyze the limitations of the amplification of the anomalous Hall deviation in Bloch oscillations due to the wave-packet expansion and show that the AHE deviation $\Delta y_{\text{AHE},D}(t)$ always remains smaller than the wave packet size $\sigma(t)$. We consider the Dirac Hamiltonian, supposing that it describes now a single valley in a periodic system. Usually, the Brillouin zone contains a small number of such valleys (for example, two). Moreover, the Berry curvature, determining the AHE deviation, and the mass, determining the wave-packet growth speed, are generally not independent: the flatter is the band (higher mass), the broader is the distribution of the Berry curvature. In other words, if the Berry curvature is strongly localized (narrow valley), the mass in this valley is necessarily smaller with respect to the case when the Berry curvature is not localized. For the particular case of the Dirac Hamiltonian, the corresponding relations can be written as $B(0) = \alpha^2/2\Delta^2$ and $m = \hbar^2\Delta/\alpha^2$.

The broadening of a Gaussian wave packet is determined by the mass and by the initial size of this wave packet $a = 2\sigma(0)$:

$$\sigma(t) = \frac{a}{2} \sqrt{1 + \frac{4\hbar^2 t^2}{m^2 a^4}}. \quad (\text{C1})$$

For small t , it behaves as a constant plus a small correction:

$$\sigma(t) \approx a/2 + \hbar^2 t^2 / a^3 m^2, \quad (\text{C2})$$

while for large t it behaves as

$$\sigma(t) \approx \frac{\hbar t}{ma} + \frac{a^3 m}{8\hbar t}, \quad (\text{C3})$$

which means that its asymptote is a straight line $\sigma(t) \approx \hbar t / ma$ starting from the origin of the coordinates due to the vanishing vertical shift $\approx t^{-1}$. The boundary between the two limits is determined by $t_1 = ma^2 / 2\hbar$.

We consider the usual AHE configuration: a constant potential gradient ξ along x ($U = -\xi x$), which gives a linear increase of the wave vector $k_x(t) = \xi t / \hbar$. In a periodic system, this linear increase leads to Bloch oscillations in real space. The period of these oscillations T can be found from the Brillouin zone size, which cannot be smaller than the Berry curvature localization scale w_B determined by the fact that the integral of the Berry curvature (the Chern number) needs to be an integer (usually of the order of one): $B(0)w_B^2 \approx 1$. Therefore, $w_B \sim 1/\sqrt{B(0)} \sim \Delta/\alpha$.

When the wave packet crosses the Brillouin zone once, it gains an AHE deviation of $\Delta y_{\text{AHE}} \sim \alpha/\Delta$. Over a certain time t , the total AHE deviation is therefore

$$\Delta y_{\text{AHE}} \sim \frac{\alpha}{\Delta} \frac{t}{T}, \quad (\text{C4})$$

where t/T is the number of Brillouin zones crossed by the wave packet during the time t . This is a straight line starting from the origin of the coordinates. If we wish to have an AHE

deviation larger than the wave packet size, this straight line needs to cross the curve for $\sigma(t)$ [Eq. (C1)]. This can occur either in the flat part of $\sigma(t)$ ($t < t_1$), or in the linearly growing part of $\sigma(t)$, provided that the slope of Δy_{AHE} is higher than that of $\sigma(t)$: $\alpha/\Delta T > \hbar/ma$. Both of these inequalities lead to the same condition for the potential gradient:

$$\xi > \frac{\Delta}{a}, \quad (\text{C5})$$

which qualitatively means that the potential gradient needs to be so large, that the potential difference between the two edges of the wave packet is equal to the size of the gap between the bands. This is clearly incompatible with the adiabaticity and even with the semiclassical description, which requires the changes to be small at the scale of the wave packet. We therefore conclude that it is impossible to obtain an AHE deviation exceeding the wave packet size using the AHE amplification provided by the Bloch oscillations, contrary to the 2D harmonic trap case considered in the main text, where the wave packet size remains fixed thanks to the properties of the harmonic oscillator.

APPENDIX D: NONADIABATICITY AND ANHARMONICITY

The quantum metric was introduced in the 1980 as an effort to find a meaningful metric tensor for quantum states, allowing to determine distances between them independently of the gauge [71]. The distance between quantum states is linked with their overlap as $ds^2 = 1 - |\langle \psi(\mathbf{k}) | \psi(\mathbf{k} + d\mathbf{k}) \rangle|^2$ and it can be expressed via the quantum metric as $ds^2 = \sum_{ij} g_{ij} dk_i dk_j$, where \mathbf{k} is a vector of parameters determining the eigenstates of a Hamiltonian (for example, a wave vector). The quantum metric can be found from the following expression:

$$g_{ij} = \text{Re} \left[\left\langle \frac{\partial \psi}{\partial k_i} \left| \frac{\partial \psi}{\partial k_j} \right\rangle - \left\langle \psi \left| \frac{\partial \psi}{\partial k_i} \right\rangle \left\langle \frac{\partial \psi}{\partial k_j} \left| \psi \right\rangle \right]. \quad (\text{D1})$$

Qualitatively, the metric allows us to find the variation of the eigenstate as a function of the variation of parameters [80]. If the separation in the parameter (wave vector) space is finite, the overlap between the eigenstates ψ_1 and ψ_2 can be found by integration of the metric:

$$I = 1 - \left(\int_{|\psi_1\rangle}^{|\psi_2\rangle} \sqrt{\sum_{ij} g_{ij} dk_i dk_j} \right)^2, \quad (\text{D2})$$

where the integral should be taken along a geodesic. This overlap shows up in many dynamical effects, such as interband transitions and oscillations due to excitation of several bands [36]. In our case, this integral of the quantum metric appears in the expression for the nonadiabatic fraction appearing due to interband transitions caused by finite velocity in the parameter (reciprocal) space [70,81,82]:

$$f_{\text{NA}} = \left(\int_{k_1}^{k_2} \sqrt{\sum_{ij} g_{ij} dk_i dk_j} \right)^2. \quad (\text{D3})$$

It gives an upper bound on the nonadiabatic fraction, since it provides an overlap between the eigenstate of one band at

wave vector k_1 (for example, $k = 0$) with the eigenstate of another band at wave vector k_2 (for example, $k = k_{\max}$).

First, we provide the expression for the quantum metric in the Dirac Hamiltonian, obtained from its eigenstates using Eq. (D1):

$$g_{kk} = \frac{\alpha^2}{4(\Delta^2 + \alpha^2 k^2)}. \quad (\text{D4})$$

The low-wave-vector limit of this expression is used for the calculation of nonadiabatic fraction in the main text. Indeed, the quantum metric of the Dirac Hamiltonian is constant in this approximation, and the integral (D3) becomes simply a product:

$$\sqrt{f_{NA}} = \int_0^{k_{\max}} \sqrt{\sum_{ij} g_{ij} dk_i dk_j} \approx \sqrt{g_{kk}(0)} k_{\max}. \quad (\text{D5})$$

This expression is used in the main text.

We also note that the calculation of anharmonicity for the Dirac case gives exactly the same result for Q as the calculation of nonadiabaticity, because there is no independent mass in the Dirac equation: everything is determined by the interplay of Δ and αk .

We now compare the contributions of nonadiabaticity and anharmonicity for the TE-TM case, where both can potentially be important. The calculation of anharmonicity is presented in the main text. The calculation of nonadiabaticity follows the same lines as the one presented in the main text for the Dirac case.

The quantum metric for the TE-TM Hamiltonian, obtained from its eigenstates using Eq. (D1), reads

$$g_{kk} = \frac{\Delta^2 \beta^2 k^2}{(\Delta^2 + \beta^2 k^4)^2}, \quad (\text{D6})$$

which for small wave vectors can be approximated as

$$g_{kk} \approx \frac{\beta^2 k^2}{\Delta^2}. \quad (\text{D7})$$

The approximation based on Eq. (D3) for the nonadiabatic fraction reads

$$\sqrt{f_{NA}} \approx \int_0^{k_{\max}} \sqrt{g_{kk}} dk \approx \frac{\beta k_{\max}^2}{2\Delta}. \quad (\text{D8})$$

The corresponding Q factor (the inverse of the nonadiabatic fraction) reads

$$Q_1 = \frac{4\Delta^2 \hbar^4}{\beta^2 \xi^2 m^2 x_0^4}, \quad (\text{D9})$$

whereas the Q factor due to anharmonicity, found in the main text, reads

$$Q_2 \approx \frac{\hbar^4 \Delta}{6\beta^2 m^2 \xi x_0^2}. \quad (\text{D10})$$

Their ratio is

$$\frac{Q_1}{Q_2} = \frac{12\Delta}{\xi x_0^2/2}. \quad (\text{D11})$$

As we see, it depends on the ratio between the Zeeman splitting and the initial potential energy of the wave packet in the

harmonic oscillator, with an extra factor 12. The smaller is the initial deviation x_0 , the larger is Q_1 with respect to Q_2 . For the parameters presented in the main text, the ratio $Q_1/Q_2 \gg 1$, which is why we neglect the losses due to the nonadiabaticity in the main text. For larger x_0 , everything becomes more complicated, but the most important role is played by the critical value of x_0 beyond which Q drops very quickly.

APPENDIX E: LIMITATIONS OF THE PERTURBATIVE TREATMENT

The condition for the application of the perturbation theory is that the scale of the corrections should be much smaller than the distance between the levels of the 2D harmonic-oscillator potential. The rapid decrease of Q^D for large x_0 is due to the resonant effect of the perturbation, exceeding this limit. In the main text, we wrote the full system Hamiltonian as $H = U + H_{\text{SOC}}$ where the kinetic-energy term was included in $H_{\text{SOC}} = H_{\text{kin}} + V_{\text{SOC}}$. This decomposition of H_{SOC} is straightforward in the TE-TM case, and less easy for the Dirac Hamiltonian. It can nevertheless be done, and we are now going to assume that V_{SOC} is a perturbation whose scale is determined by the maximal wave vector k_{\max} . This perturbation leads to a resonant transfer between the states if its energy scale becomes equal to the splitting between the harmonic-oscillator states $\hbar\omega$, which can be written as the following condition:

$$\sqrt{\alpha^2 k_{\max}^2 + \Delta_D^2} - \left(\Delta_D + \frac{\alpha^2 k_{\max}^2}{2\Delta_D} \right) = \hbar\omega, \quad (\text{E1})$$

where the mass of the particle is $m = \hbar^2 \Delta / \alpha^2$, which gives $\hbar\omega = \alpha \sqrt{\xi} / \Delta$. Solving this equation for k_{\max} and converting it to x_0 gives $x_{\text{crit}} \approx 64 \mu\text{m}$ (the analytical expressions are quite cumbersome), which is exactly what we see in numerical simulations.

For TE-TM, similar to the case of the Dirac Hamiltonian, a cutoff for Q is with a very high precision determined by the resonant anharmonicity condition $E(k_{\max}) - E_{h.o.}(k_{\max}) = \hbar\omega$, which reads

$$\sqrt{\Delta^2 + \beta^2 k^4} - \Delta = \hbar\omega. \quad (\text{E2})$$

This constraint leads to the strong decrease of the rotation angles $\phi_{1/2}$ and ϕ for large x_0 .

We conclude that one should reduce Δ to maximize the maximal rotation angle, whereas x_0 can be kept as large as possible below the critical value in order to improve the observability of the oscillations.

APPENDIX F: UNCERTAINTY

The finesse of the oscillator Q is also the measure of the improvement of the precision of the measurement of the Berry curvature B . Indeed, the relative uncertainty of the anomalous Hall deviation $\delta(\Delta y) / \Delta y$ determines the uncertainty on the Berry curvature $\delta B / B$. The amplification of the deviation in the Foucault pendulum configuration increases the denominator of the first fraction by a factor Q , thus reducing the uncertainty on the Berry curvature by the same factor. This would mean reducing the 10% uncertainty on the Berry curvature in Ref. [36] down to 0.1% with $Q = 100$ from Fig. 3 of

the main text, a significant improvement. However, Q should be maximized not by reducing x_0 , but rather by reducing Δ . The limit to this improvement is set by $\Delta > \beta/\sigma^2 = 4\pi^2\beta\sqrt{\xi m}/\hbar$ (wave packet size should be smaller than the Berry curvature variation scale), around 1 μeV .

APPENDIX G: DETERMINATION OF BERRY CURVATURE PROFILE

In the main text, we show that the Berry-Foucault pendulum allows finding with high precision the Berry curvature at low wave vectors. In this section, we demonstrate that the knowledge of the Berry curvature at low wave vectors gives a full description of the profile of the Berry curvature for a known Hamiltonian type.

In the Dirac Hamiltonian, the Berry curvature is given by

$$B_z^D(k) = \frac{\alpha^2 \Delta_D}{2(\alpha^2 k^2 + \Delta_D^2)^{3/2}}, \quad (\text{G1})$$

and the Berry curvature at low wave vector is given by $B^0 = \alpha^2/2\Delta^2$. It is easy to show that the Berry curvature $B(k)$ can be written as a single-parameter function of k , with this single parameter being precisely B^0 :

$$B(k) = \frac{B^0}{(1 + B^0 k^2/2)^{3/2}}, \quad (\text{G2})$$

because its integral is normalized (the Chern number). It means that measuring B^0 with a high precision allows one to find the whole distribution of the Berry curvature with the same precision.

In the TE-TM Hamiltonian, the Berry curvature is given by

$$B_z^{\text{TE-TM}}(k) = \frac{2\Delta\beta^2 k^2}{(\Delta^2 + \beta^2 k^4)^{3/2}}, \quad (\text{G3})$$

and its low-wave-vector approximation is $B^0(k) = \eta k^2$, $\eta = 2\beta^2/\Delta^2$ being the quantity we determine with high precision with the Berry-Foucault pendulum. It is again straightforward to show that the Berry curvature in this case can also be

written as a single-parameter function of k , with the single parameter η :

$$B(k) = \frac{\eta k^2}{(1 + \eta k^4/2)^{3/2}}. \quad (\text{G4})$$

Thus, the Berry-Foucault pendulum allows determining the whole Berry curvature distribution in the case of TE-TM as well.

APPENDIX H: LARGE-AMPLITUDE OSCILLATIONS

Here, we discuss the case of $k_{\text{max}} \rightarrow \infty$. This regime is subject to strong nonadiabaticity due to the possibility of resonant transitions between the harmonic-oscillator states. Nevertheless, one can imagine that the maximal value of the AHE drift is achieved for k below this critical condition. Indeed, the maximal AHE drift is

$$\Delta y^{\text{max}} = \sqrt{\frac{\beta}{\Delta}} \frac{\Gamma^2(3/4)}{\sqrt{\pi}}. \quad (\text{H1})$$

It is achieved when $k_{\text{max}} \gg k^* = \sqrt{\Delta/\beta}$, which is the wave vector of maximal Berry curvature, which gives $x_0 \gg \hbar\sqrt{\Delta}/\sqrt{\beta\xi m}$. For large $\hbar\omega$, this wave vector could be accessible. The maximal angle of rotation before desynchronization in this limit is

$$\phi_{\text{max}}^{\infty} = \frac{y_{\text{AHE}}^{\text{max}}}{x_0} \ll \frac{\beta}{\Delta} \frac{\sqrt{\xi m}}{\hbar} \frac{\Gamma^2(3/4)}{\sqrt{\pi}}. \quad (\text{H2})$$

However, the width of the wave packet in the harmonic oscillator is $l^2 = \hbar/\sqrt{\xi m}$. Requiring the expression on the right to be much larger than unity, we obtain $l \ll 2\pi/k^*$, and considering that l determines the size of the wave packet in the reciprocal space, $\Delta k \gg k^*$, which means that the wave packet has to be so small in real space and so large in reciprocal space, that the semiclassical theory is inapplicable. The limit $k_{\text{max}} \rightarrow \infty$ is therefore impossible to combine with large rotation angles in a harmonic oscillator in the adiabatic regime, and thus the low- k limit considered in the main text is the most relevant.

-
- [1] L. Foucault, *C. R. Hebd. Séances Acad. Sci. Paris* **32**, 135 (1851).
- [2] M. F. Conlin, *Isis* **90**, 181 (1999).
- [3] J. Oprea, *Am. Math. Mon.* **102**, 515 (1995).
- [4] P. Gilbert, *Bull. Sci. Math. Astron.* **2e Série** **6**, 189 (1882).
- [5] J. Sommeria, *C. R. Phys.* **18**, 520 (2017).
- [6] N. D. Lane, E. Miluzzo, H. Lu, D. Peebles, T. Choudhury, and A. T. Campbell, *IEEE Commun. Mag.* **48**, 140 (2010).
- [7] N. S. Bedrossian, S. Bhatt, W. Kang, and I. M. Ross, *IEEE Control Syst. Mag.* **29**, 53 (2009).
- [8] N. Yazdi, F. Ayazi, and K. Najafi, *Proc. IEEE* **86**, 1640 (1998).
- [9] P. Shao, C. L. Mayberry, X. Gao, V. Tavassoli, and F. Ayazi, *J. Microelectromech. Syst.* **23**, 762 (2014).
- [10] I. P. Prikhodko, S. A. Zotov, A. A. Trusov, and A. M. Shkel, *Sens. Actuators, A* **177**, 67 (2012).
- [11] C. Qu and S. Stringari, *Phys. Rev. Lett.* **120**, 183202 (2018).
- [12] A. Shapere and F. Wilczek, *Geometric Phases in Physics* (World Scientific, Singapore, 1989).
- [13] J. H. Hannay, *J. Phys. A: Math. Gen.* **18**, 221 (1985).
- [14] M. V. Berry, *J. Phys. A: Math. Gen.* **18**, 15 (1985).
- [15] A. Kheif and D. F. Nelson, *Am. J. Phys.* **61**, 170 (1993).
- [16] J. von Bergmann and H. von Bergmann, *Am. J. Phys.* **75**, 888 (2007).
- [17] P. Delplace and A. Venaille, *C. R. Phys.* **21**, 165 (2020).
- [18] V. B. Braginsky, A. G. Polnarev, and K. S. Thorne, *Phys. Rev. Lett.* **53**, 863 (1984).
- [19] M. P. Cartmell, J. E. Faller, N. A. Lockerbie, and E. Handous, *Proc. R. Soc. London, Ser. A* **476**, 20190680 (2020).
- [20] A. Einstein, *Jahrb. Radioakt.* **4**, 411 (1907).
- [21] S. Pantcharatnam, *Proc. Indian Acad. Sci. A* **44**, 247 (1956).
- [22] M. V. Berry, *Proc. R. Soc. London, Ser. A* **392**, 45 (1984).
- [23] M. V. Berry, in *Geometric Phases in Physics*, edited by A. Shapere and F. Wilczek (World Scientific, Singapore, 1989), p. 7.
- [24] M. Onoda, S. Murakami, and N. Nagaosa, *Phys. Rev. Lett.* **93**, 083901 (2004).

- [25] K. Bliokh and Y. Bliokh, *Phys. Lett. A* **333**, 181 (2004).
- [26] A. Kavokin, G. Malpuech, and M. Glazov, *Phys. Rev. Lett.* **95**, 136601 (2005).
- [27] K. Y. Bliokh, Y. Gorodetski, V. Kleiner, and E. Hasman, *Phys. Rev. Lett.* **101**, 030404 (2008).
- [28] M. König, S. Wiedmann, C. Brune, A. Roth, H. Buhmann, L. W. Molenkamp, X.-L. Qi, and S.-C. Zhang, *Science* **318**, 766 (2007).
- [29] D. Hsieh, D. Qian, L. Wray, Y. Xia, Y. S. Hor, R. J. Cava, and M. Z. Hasan, *Nature (London)* **452**, 970 (2008).
- [30] M. Z. Hasan and C. L. Kane, *Rev. Mod. Phys.* **82**, 3045 (2010).
- [31] B. Bahari, A. Ndao, F. Vallini, A. El Amili, Y. Fainman, and B. Kanté, *Science* **358**, 636 (2017).
- [32] D. D. Solnyshkov, O. Bleu, and G. Malpuech, *Appl. Phys. Lett.* **112**, 031106 (2018).
- [33] D. Karki, R. El-Ganainy, and M. Levy, *Phys. Rev. Appl.* **11**, 034045 (2019).
- [34] N. Nagaosa, X. Yu, and Y. Tokura, *Philos. Trans. R. Soc., A* **370**, 5806 (2012).
- [35] G. Sundaram and Q. Niu, *Phys. Rev. B* **59**, 14915 (1999).
- [36] A. Gianfrate, O. Bleu, L. Dominici, V. Ardizzone, M. De Giorgi, D. Ballarini, G. Lerario, K. West, L. Pfeiffer, D. Solnyshkov, D. Sanvitto, and G. Malpuech, *Nature (London)* **578**, 381 (2020).
- [37] Y. A. Bychkov and É. I. Rashba, *Pis'ma Zh. Eksp. Teor. Fiz.* **39**, 66 (1984) [*JETP Lett.* **39**, 78 (1984)].
- [38] R. Winkler, U. Zülicke, and J. Bolte, *Phys. Rev. B* **75**, 205314 (2007).
- [39] W. Zawadzki and T. M. Rusin, *J. Phys.: Condens. Matter* **23**, 143201 (2011).
- [40] D. Xiao, G.-B. Liu, W. Feng, X. Xu, and W. Yao, *Phys. Rev. Lett.* **108**, 196802 (2012).
- [41] G. Wang, A. Chernikov, M. M. Glazov, T. F. Heinz, X. Marie, T. Amand, and B. Urbaszek, *Rev. Mod. Phys.* **90**, 021001 (2018).
- [42] L. Ju, Z. Shi, N. Nair, Y. Lv, C. Jin, J. Velasco, C. Ojeda-Aristizabal, H. A. Bechtel, M. C. Martin, A. Zettl, James Analytis, and Feng Wang, *Nature (London)* **520**, 650 (2015).
- [43] J. Noh, S. Huang, K. P. Chen, and M. C. Rechtsman, *Phys. Rev. Lett.* **120**, 063902 (2018).
- [44] K. Y. Bliokh, A. Niv, V. Kleiner, and E. Hasman, *Nat. Photonics* **2**, 748 (2008).
- [45] C. P. Jisha and A. Alberucci, *J. Opt. Soc. Am. A* **34**, 2019 (2017).
- [46] Z. Zhang, S. Liang, F. Li, S. Ning, Y. Li, G. Malpuech, Y. Zhang, M. Xiao, and D. Solnyshkov, *Optica* **7**, 455 (2020).
- [47] C. Leyder, M. Romanelli, J. P. Karr, E. Giacobino, T. C. Liew, M. M. Glazov, A. V. Kavokin, G. Malpuech, and A. Bramati, *Nat. Phys.* **3**, 628 (2007).
- [48] R. Su, E. Estrecho, D. Biegańska, Y. Huang, M. Wurdack, M. Pieczarka, A. G. Truscott, T. C. H. Liew, E. A. Ostrovskaya, and Q. Xiong, *Sci. Adv.* **7**, eabj8905 (2021).
- [49] M. Krol, I. Septembre, P. Oliwa, M. Kedziora, K. Lempicka-Mirek, M. Muszynski, R. Mazur, P. Morawiak, W. Piecek, P. Kula *et al.*, *Nat. Commun.* **13**, 5340 (2022).
- [50] Y. M. R. Hu, E. A. Ostrovskaya, and E. Estrecho, *Phys. Rev. B* **108**, 115404 (2023).
- [51] R. Balili, V. Hartwell, D. Snoke, L. Pfeiffer, and K. West, *Science* **316**, 1007 (2007).
- [52] G. Tosi, G. Christmann, N. Berloff, P. Tsotsis, T. Gao, Z. Hatzopoulos, P. Savvidis, and J. Baumberg, *Nat. Phys.* **8**, 190 (2012).
- [53] H. Terças, H. Flayac, D. D. Solnyshkov, and G. Malpuech, *Phys. Rev. Lett.* **112**, 066402 (2014).
- [54] L. Polimeno, G. Lerario, M. De Giorgi, L. De Marco, L. Dominici, F. Todisco, A. Coriolano, V. Ardizzone, M. Pugliese, C. T. Prontera *et al.*, *Nat. Nanotechnol.* **16**, 1349 (2021).
- [55] M.-C. Chang and Q. Niu, *J. Phys.: Condens. Matter* **20**, 193202 (2008).
- [56] M. Baktavatsalou, *J. Phys. Radium* **22**, 159 (1961).
- [57] X. Xu, W. Yao, D. Xiao, and T. F. Heinz, *Nat. Phys.* **10**, 343 (2014).
- [58] I. A. Shelykh, G. Pavlovic, D. D. Solnyshkov, and G. Malpuech, *Phys. Rev. Lett.* **102**, 046407 (2009).
- [59] G. Barenboim and J. Oteo, *Eur. J. Phys.* **34**, 1049 (2013).
- [60] The parameters used in numerical simulations for Fig. 2 were the polariton mass $m = 5 \times 10^{-5} m_0$ (m_0 is the free electron mass), polariton lifetime $\tau = 300$ ps, $\Delta = 0.1$ meV, $\beta = 270 \mu\text{eV } \mu\text{m}^2$, $\xi = 1.6 \times 10^{-13}$ N/m. The simulations were carried out using the 3rd-order Adams method for the time derivative and a GPU-accelerated FFT for the Laplacian.
- [61] S. Klemmt, T. Harder, O. Egorov, K. Winkler, R. Ge, M. Bandres, M. Emmerling, L. Worschech, T. Liew, M. Segev, C. Schneider, and S. Höfling, *Nature (London)* **562**, 552 (2018).
- [62] C. Cohen-Tannoudji, B. Diu, F. Laloe, *Quantum Mechanics*, Vol. 1 (Wiley-VCH, New York, 1986).
- [63] M. O. Scully and M. S. Zubairy, *Quantum Optics* (Cambridge University Press, Cambridge, 1999).
- [64] K. Leo, P. H. Bolivar, F. Brüggemann, R. Schwedler, and K. Köhler, *Solid State Commun.* **84**, 943 (1992).
- [65] M. Ben Dahan, E. Peik, J. Reichel, Y. Castin, and C. Salomon, *Phys. Rev. Lett.* **76**, 4508 (1996).
- [66] Z. A. Geiger, K. M. Fujiwara, K. Singh, R. Senaratne, S. V. Rajagopal, M. Lipatov, T. Shimasaki, R. Driben, V. V. Konotop, T. Meier, and David M. Weld, *Phys. Rev. Lett.* **120**, 213201 (2018).
- [67] H. Trompeter, W. Krolikowski, D. N. Neshev, A. S. Desyatnikov, A. A. Sukhorukov, Y. S. Kivshar, T. Pertsch, U. Peschel, and F. Lederer, *Phys. Rev. Lett.* **96**, 053903 (2006).
- [68] The parameters used in numerical simulations for Fig. 3 were, for the Dirac Hamiltonian: $\alpha = 2$ meV μm , $\Delta_D = 2$ meV, $\xi = 7.8e - 14$ N/m. For the TE-TM Hamiltonian they were the polariton mass $m = 2 \times 10^{-5} m_0$ (m_0 is the free electron mass), polariton lifetime $\tau = 300$ ps, $\Delta = 0.24$ meV, $\beta = 135 \mu\text{eV } \mu\text{m}^2$, $\xi = 4.4 \times 10^{-13}$ N/m. The simulations were carried out using the 3rd-order Adams method for the time derivative and a GPU-accelerated FFT for the Laplacian.
- [69] E. O. Schulz-DuBois, *Am. J. Phys.* **38**, 173 (1970).
- [70] O. Bleu, G. Malpuech, Y. Gao, and D. D. Solnyshkov, *Phys. Rev. Lett.* **121**, 020401 (2018).
- [71] J. Provost and G. Vallee, *Commun. Math. Phys.* **76**, 289 (1980).
- [72] E. Wertz, A. Amo, D. D. Solnyshkov, L. Ferrier, T. C. H. Liew, D. Sanvitto, P. Senellart, I. Sagnes, A. Lemaître, A. V. Kavokin, G. Malpuech, and J. Bloch, *Phys. Rev. Lett.* **109**, 216404 (2012).

- [73] L. C. Camenzind, L. Yu, P. Stano, J. D. Zimmerman, A. C. Gossard, D. Loss, and D. M. Zumbühl, *Phys. Rev. Lett.* **122**, 207701 (2019).
- [74] I. Bloch, J. Dalibard, and W. Zwerger, *Rev. Mod. Phys.* **80**, 885 (2008).
- [75] D. M. Harber, J. M. Obrecht, J. M. McGuirk, and E. A. Cornell, *Phys. Rev. A* **72**, 033610 (2005).
- [76] H. M. Price and N. R. Cooper, *Phys. Rev. A* **85**, 033620 (2012).
- [77] H. M. Price, O. Zilberberg, T. Ozawa, I. Carusotto, and N. Goldman, *Phys. Rev. B* **93**, 245113 (2016).
- [78] M. Wimmer, H. M. Price, I. Carusotto, and U. Peschel, *Nat. Phys.* **13**, 545 (2017).
- [79] L. McIntyre, *Nature (London)* **596**, 165 (2021).
- [80] Q. Liao, C. Leblanc, J. Ren, F. Li, Y. Li, D. Solnyshkov, G. Malpuech, J. Yao, and H. Fu, *Phys. Rev. Lett.* **127**, 107402 (2021).
- [81] Y. Gao, S. A. Yang, and Q. Niu, *Phys. Rev. Lett.* **112**, 166601 (2014).
- [82] Y. Gao, S. A. Yang, and Q. Niu, *Phys. Rev. B* **95**, 165135 (2017).